AGU PUBLICATIONS

JGR

Journal of Geophysical Research: Space Physics

RESEARCH ARTICLE
10.1002/2014JA020712

Key Points:
- Four ring current model results are statistically compared to geomagnetic indices
- Results are examined as a function of solar wind driver and storm intensity
- Storm time geomagnetic response is different between ICMEs and CIRs

Correspondence to:
R. M. Katus,
rkatus@umich.edu

Citation:
Katus, R. M., M. W. Liemohn, E. L. Ionides, R. Ilie, D. Welling, and L. K. Sarno-Smith (2015), Statistical analysis of the geomagnetic response to different solar wind drivers and the dependence on storm intensity, *J. Geophys. Res. Space Physics*, *120*, 310–327, doi:10.1002/2014JA020712.

Received 10 OCT 2014
Accepted 23 NOV 2014
Accepted article online 4 DEC 2014
Published online 22 JAN 2015

Statistical analysis of the geomagnetic response to different solar wind drivers and the dependence on storm intensity

R. M. Katus[1,2], M. W. Liemohn[1], E. L. Ionides[1], R. Ilie[1], D. Welling[1], and L. K. Sarno-Smith[1]

[1]Department of Atmospheric, Oceanic and Space Sciences, University of Michigan, Ann Arbor, Michigan, USA, [2]Department of Physics and Astronomy, West Virginia University, Morgantown, West Virginia, USA

Abstract Geomagnetic storms start with activity on the Sun that causes propagation of magnetized plasma structures in the solar wind. The type of solar activity is used to classify the plasma structures as being either interplanetary coronal mass ejection (ICME) or corotating interaction region (CIR) driven. The ICME-driven events are further classified as either magnetic cloud (MC) driven or sheath (SH) driven by the geoeffective structure responsible for the peak of the storm. The geoeffective solar wind flow then interacts with the magnetosphere producing a disturbance in near-Earth space. It is commonly believed that a SH-driven event behaves more like a CIR-driven event than a MC-driven event; however, in our analysis this is not the case. In this study, geomagnetic storms are investigated statistically with respect to the solar wind driver and the intensity of the events. We use the Hot Electron and Ion Drift Integrator (HEIDI) model to simulate the inner magnetospheric hot ion population during all of the storms classified as intense ($Dst_{min} \leq -100$ nT) within solar cycle 23 (1996–2005). HEIDI is configured four different ways using either the Volland-Stern or self-consistent electric field and either event-based Los Alamos National Laboratory (LANL) magnetospheric plasma analyzer (MPA) data or a reanalyzed lower resolution version of the data that provides spatial resolution. Presenting the simulation results, geomagnetic data, and solar wind data along a normalized epoch timeline shows the average behavior throughout a typical storm of each classification. The error along the epoch timeline for each HEIDI configuration is used to rate the model's performance. We also subgrouped the storms based on the magnitude of the minimum *Dst*. We found that typically the LANL MPA data provide the best outer boundary condition. Additionally, the self-consistent electric field better reproduces SH- and MC-driven events throughout most of the storm timeline, but the Volland-Stern electric field better reproduces CIR-driven events. Contrary to what we expect, examination of the HEIDI model results and solar wind data shows that SH-driven events behave more like MC-driven events than CIR-driven storms.

1. Introduction

A geomagnetic storm is a disturbance in near-Earth space caused by the geoeffective solar wind flow that results from activity on the Sun. The two most geoeffective solar wind structures can be categorized as either a corotating interaction region (CIR) or an interplanetary coronal mass ejection (ICME) depending upon the solar source. A CIR is affiliated with high-speed solar wind originating from solar coronal holes. This geoeffective structure forms where the leading edge of the high-speed stream interacts with the preceding slower solar wind. In this interaction region, the plasma is heated and compressed. An ICME is affiliated with compressed sheath fields, ejecta from the corona, or some combination of these two structures. A detailed description of the combination of solar wind structures is given in *Yue and Zong* [2011]. In the sheath (SH) region solar wind plasma can be described like a CIR. The plasma is heated and compressed. The storms containing sheath regions (like CIRs) are typically associated with rapidly varying magnetic field direction and high dynamic pressure. Therefore, SH-driven geomagnetic storms should have a main phase similar to a CIR-driven main phase. Of the two types of ICME structures, some events may also contain magnetic clouds (MC). The storms containing MC are a subset of ICME storms, which are associated with a strong magnetic field that is rotated through a large angle [e.g., *Klein and Burlaga*, 1982; *Lepping et al*., 1990; *Mulligan et al*., 1998; *Lynch et al*., 2003].

The geospace response to ICME and CIR forcing has been shown to be very different. *Tsurutani and Gonzalez* [1997] reviewed these differences in a comprehensive assessment of these two types of events. *Kataoka and Miyoshi* [2006] showed that the solar wind properties of the shock downstream and stream interface are very different, and *Miyoshi and Kataoka* [2005] showed that the responses of the inner magnetosphere are also very different. Additionally, *Borovsky and Denton* [2006] provided a comparison of the magnetospheric response to each of the drivers. Inner magnetospheric simulations have been used to show drift physics models better reproduce ICME-driven events than CIR-driven events [e.g., *Jordanova*, 2006; *Jordanova et al*., 2009].

Liemohn et al. [2010] presented simulation results for all 90 intense geomagnetic events of solar cycle 23 using the Hot Electron and Ion Drift Integrator (HEIDI) model, employing different outer boundary conditions and electric field descriptions. Their study examined the effect of different solar wind drivers on the inner magnetospheric hot ion population. They examined the peak of the storms and found HEIDI consistently underpredicted the peak *Dst** for CIR-driven events while matching the dayside plasma observations relatively well. This implies there are other currents contributing to the low-latitude magnetic perturbations preferentially during CIR-driven events compared to ICME-driven events.

Liemohn and Katus [2012] used the same simulation set as *Liemohn et al*. [2010] for a statistical analysis of the similarities and differences throughout ICME- and CIR-driven storms. Their data-model comparisons used the *SYM-H** index, a higher-resolution index similar to *Dst**, but that one is calculated slightly differently using data from magnetometers that extend to midlatitudes. Their comparisons include the entire collections of events using superposed epoch analysis. They found that for ICME-driven events, the simulations that used a self-consistent electric field description had a lower root-mean-square error (RMSE) and higher correlation than a simple Volland-Stern electric field [*Volland*, 1973; *Stern*, 1975]. But during CIR-driven events, the simple electric field model better replicated the events. Therefore, they infer that CIR-driven events respond strongly to transient spikes in the plasma outer boundary condition, while ICME passages exhibit a more highly structured electric field.

The magnitude of the *Dst** index is a factor that increases root-mean-square error (RMSE). The RMSE is biased by the large differences. This study further subgroups the geomagnetic disturbances based on the storm peak magnitude. This subgrouping allows investigation of dependence of the previous results on the storm peak magnitude and a more direct comparison of each of the storm driver categories.

While CIR and sheath-driven structures have different sources, the theoretical description of these solar wind structures is the same. In the leading edge of a CIR and sheath structure, plasma is heated and compressed, while the magnetic field varies rapidly. In this study we examine the inner magnetospheric response to these solar wind structures during the main phase of the storm. To analyze the main phase dynamics we use numerical simulations of the inner magnetosphere as well as solar wind, geosynchronous, and ground-based data. The storms are also subgrouped based on their minimum *Dst*. It is shown that LANL MPA data are required to provide the best outer boundary condition. Additionally, in contrast to what we expect, examination of the HEIDI model results and solar wind data shows that SH-driven events behave more like MC-driven events than CIR-driven storms.

2. The Model

The Hot Electron and Ion Drift Integrator (HEIDI) models the ring current by solving the gyration and bounce-averaged kinetic equation for phase space density of the inner magnetospheric hot-charged particle populations [*Liemohn et al*., 2001a]. The HEIDI model is based on the ring current-atmosphere interaction model (RAM) described by *Fok et al*. [1995] and *Jordanova et al*. [1996]. The spatial domain used in the HEIDI model extends from 1.875 R_E to 6.625 R_E. The model version that is used in this study assumes a static dipole magnetic field for simplicity and computational tractability. HEIDI uses the *Rairden et al*. [1986] neutral hydrogen density model, needed to calculate the charge exchange collisional losses between the hot ring current ions and the cold geocorona. Note that the latest modifications to HEIDI include a generalized formalism that allows nondipolar magnetic fields [*Ilie et al*., 2012] and additional geocoronal model [*Ilie et al*., 2012]. HEIDI is also coupled to the Dynamic Global Core Plasma Model [*Ober et al*., 1997] to simulate the plasmasphere [*Liemohn et al*., 2004], which is needed for Coulomb collisional scattering and decay.

Table 1. HEIDI Run Set Configurations

	Volland-Stern Electric Field	Self-Consistent Electric Field
LANL MPA outer boundary	1	2
Reanalyzed LANL outer boundary	3	4

The electric field used in HEIDI can be specified. In this study, the electric field is given by a Volland-Stern electric field [*Volland*, 1973; *Stern*, 1975] and a self-consistent electric field [*Liemohn et al*., 2001b, 2004; *Ridley and Liemohn*, 2002]. The Volland-Stern model is a statistically derived description of the convection electric field driven by *Kp*. This simple model provides a relatively smooth and accurate result. *Thomsen* [2004] showed that *Kp* is a good electric field driver because it is strongly influenced by the motion of the inner plasma sheet, which is determined by the intensity of magnetospheric convection.

The self-consistent electric field description is based on the particle pressures and field-aligned currents through the subauroral ionosphere with the use of a dynamically varying auroral conductance setting. While studies have shown that self-consistent electric field provides a more realistic solution, the simple Volland-Stern model was shown to better replicate CIR-driven events [*Liemohn et al*., 2010; *Liemohn and Katus*, 2012].

The outer boundary condition used in the HEIDI model for the particle populations requires information of nightside plasma parameters. For this version of HEIDI, the outer boundary is set at geosynchronous orbit for all MLTs, and the flow out the magnetopause is a function of particle energy and density during the gradient curvature drift inside of the boundary. In this study, two versions of the plasma data are employed as the outer boundary condition. The first boundary condition applies geosynchronous observations from Los Alamos National Laboratory satellites [e.g., *Thomsen et al*., 1998]. These high time resolution (96 s cadence) measurements are obtained from magnetospheric plasma analyzer (MPA) [*Bame et al*., 1993] and synchronous orbiting particle analyzer (SOPA) [*Belian et al*., 1992] measurements. These data sets are used to define the inflow along the all local times across the outer boundary. The second boundary condition applies the *O'Brien and Lemon* [2007] reanalysis of Los Alamos National Laboratory (LANL) MPA plasma density moments. These low time resolution data (1 h) provide local time variation in a 1 h MLT cadence. Both boundary conditions are modified according to the compositional split defined by *Young et al*. [1982] and implemented by *Liemohn et al*. [1999].

Table 1 describes the HEIDI run set configurations used in this study. Run sets 1 and 3 use a Volland-Stern electric field with the high time resolution plasma data for the outer boundary and the reanalyzed outer boundary condition, respectively. Run sets 2 and 4 use the self-consistent electric field with the high-resolution plasma data for the outer boundary and the reanalyzed outer boundary condition, respectively.

Liemohn and Jazowski [2008] conducted data-model comparisons at the time of the peak *Dst* using the model configuration of run set 1 for the same list of geomagnetic storms. They included 79 of the 90 storms, excluding the storms that contained gaps lasting longer than 4 h in the outer boundary condition LANL MPA data during the main phase of the storm. *Liemohn et al*. [2010] and *Liemohn and Katus* [2012] used all four run sets, plus one run set not examined in this study, to investigate the same 79 storms. The list of storms included for each run set then differed based on instability in the numerical result, caused primarily by intense localized electric fields that yield negative phase space densities.

This study includes a 4 day interval surrounding each of the 90 storms. If the model produced results for any portion of a storm, then it is used. This means that there are storms in which the modeled *Dst* just stops during the storm interval due to model runtime error. This also means that the number of data points included for each run set is different. Additionally, for each run set there is more data for the main phase than recovery phase. It should be noted that runs that use the self-consistent electric field are more likely to become unstable than runs that use the Volland-Stern electric field. Furthermore, the super storms (primarily magnetic cloud-driven and complex events) are more prone to become unstable than moderately intense events. It should also be noted that this study was recalculated using only storms with complete 4 day HEIDI runs. The differences between the two sets of results were indistinguishable in the storm time plots and in the decimal places for the statistics.

3. Event Comparison

In this study, the results from the four different HEIDI run set configurations are compared to the low latitude to midlatitude geomagnetic indices *Dst**, *SYM-H**, and United States Geological Survey (USGS) 1 min *Dst** (*USGS**). The USGS index is calculated using the same magnetometer observatories as *Dst* but using a very different method [*Love and Gannon*, 2009; *Gannon and Love*, 2011].

The disturbance storm time (*Dst*) index is a globally averaged low-latitude geomagnetic perturbation index [*Sugiura and Kamei*, 1991]. The *Dst* index is calculated from the 1 h averaged *H* component of four low-latitude magnetometers distributed in local time. A negative *Dst* is indicative of an intensification of ring current because the ring current is diamagnetic, reducing the *H* component at Earth. *Dst** is another version of the *Dst* index. The star superscript indicates that the index has been corrected to make it a better measure of perturbations related to near-Earth space currents. The correction is done for *Dst* as follows:

$$Dst^* = \frac{Dst - D_{MP} + D_Q}{C_{IC}}$$

where D_{MP} is an estimate of the contribution from the magnetopause current (defined by the upstream solar wind dynamic pressure), D_Q is the quiet time offset value, and C_{IC} is a correction factor for the contribution from the induced currents within the Earth. This correction can also be done with the 1 min counter parts of *Dst*, *SYM-H* [*Iyemori*, 1990; *Iyemori et al*., 1992], or United States Geological Survey (USGS) *Dst* [*Love and Gannon*, 2009; *Gannon and Love*, 2011; *Katus and Liemohn*, 2013].

These geomagnetic indices and their corrected format are frequently used to describe the intensity and progression of geomagnetic storms [e.g., *Gonzalez et al*., 1994]. For instance, *Burton et al*. [1975], *O'Brien and McPherron* [2000], and *Temerin and Li* [2002] provided an empirical relationship between *Dst** and the solar wind parameters. *O'Brien and McPherron* [2002] and *Zhao et al*. [2011] found that the contribution of the solar wind dynamic pressure to the disturbance in *Dst** varies with the intensity of the storm.

There were a total of 90 intense storms ($Dst_{min} \leq -100$ nT) during solar cycle 23 (1996–2005). Of these 90 intense geomagnetic events, 88 have been classified according to the solar wind driver by *Zhang et al*. [2007a, 2007b]. The two additional storms that were not part of the list by *Zhang et al*. [2007a, 2007b] occur on 17 April 2002 and 19 April 2002. These two storms are part of a large sequence of intense activity, which consists of storms on 18 April 2002 and 20 April 2002. These two events are classified as individual ICME sheath-driven events in this study because *Dst* was able to recover by more than 50 nT prior to the next event, as was discussed by *Liemohn and Jazowski* [2008].

The measure of perturbations related to near-Earth space currents in the form of any of the three geomagnetic indices can be used to quantify the HEIDI model's ability to reproduce the ring current. The Dessler-Parker-Sckopke relationship [*Dessler and Parker*, 1959; *Sckopke*, 1966] (hereinafter referred to as DPS) relates the total modeled energy of the ring current (E_{RC}) to the magnetic perturbation. The simulated quantity is described by the equation

$$DPS^*[\text{nT}] = -3.98 \times 10^{-30} E_{RC}[\text{keV}]$$

where *DPS** is the model calculation of the measured geomagnetic index.

While the direct comparison of *Dst** with *DPS** is flawed (for example, see *Liemohn* [2003] and *Ganushkina et al*. [2012] for systematic comparisons of *DPS** versus Biot-Savart integration), the link between the two is significant. Several studies have shown that *Dst* and/or *Dst** track the energy content of near-Earth hot ions during intense storms [e.g., *Greenspan and Hamilton*, 2000; *Turner et al*., 2001; *Jorgensen et al*., 2004], and numerous modeling studies have also demonstrated this close connection [e.g., *Fok et al*., 1995, 2001; *Jordanova et al*., 1996, 2001; *Ebihara and Ejiri*, 1998; *Kozyra and Liemohn*, 2003]. For instance, *Liemohn and Kozyra* [2003] quantified the similarity in the functional forms between *Dst** and *DPS**. Even though the simulation volume of HEIDI only extends to geosynchronous distance, *Liemohn* [2003] isolated the contribution of the truncation current to *DPS**, which acts as a crude proxy for the tail current contribution to this value. Even though the comparison is imperfect, it is a useful distillation that enumerates the development and helps reveal the physical processes of magnetic storms.

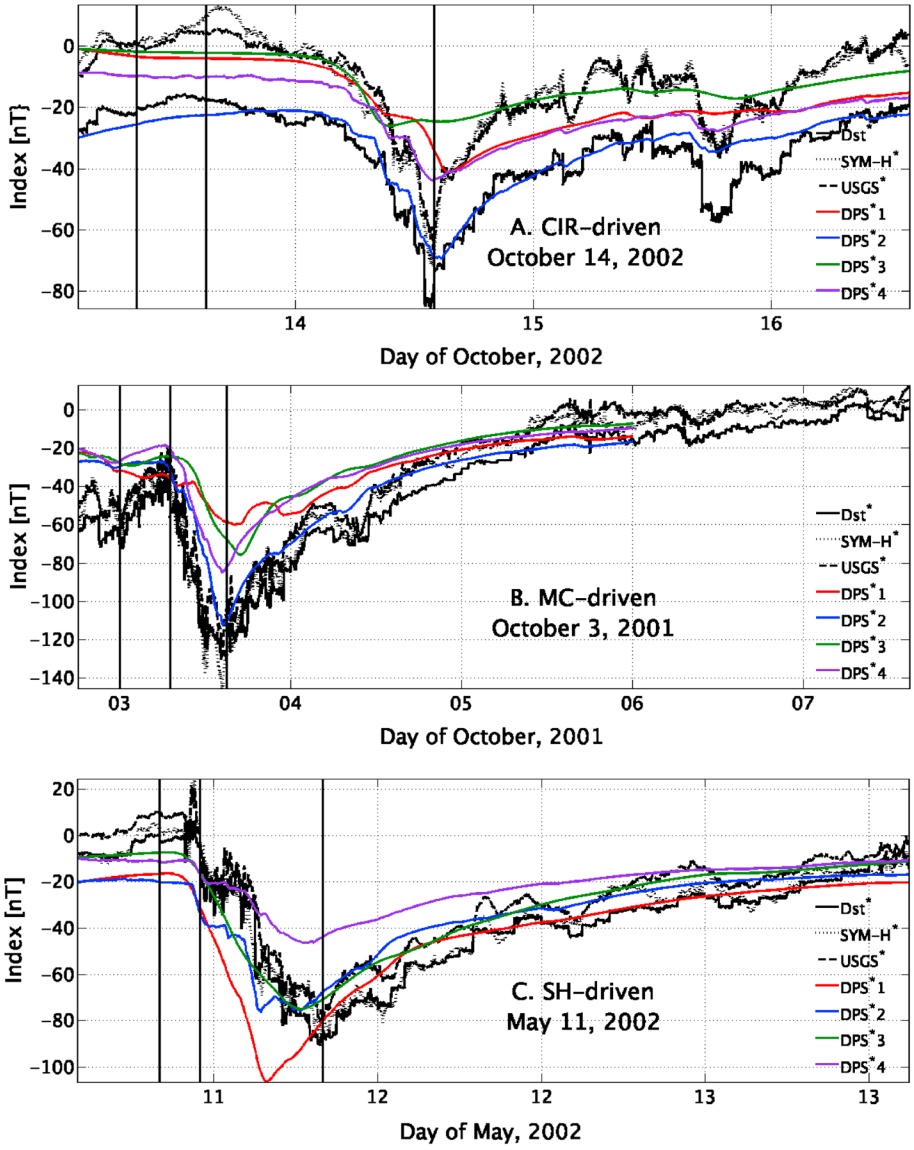

Figure 1. Example storms: (a) a CIR-driven intense storm, (b) an ICME-driven storm with the main phase caused by a magnetic cloud structure, and (c) an ICME-driven storm with the sheath as the main cause of the activity.

Three example geomagnetic storms are shown in Figure 1. Each plot in Figure 1 presents *Dst**, *SYM-H**, *USGS** and the simulated *DPS** for each of the four model run sets. All three indices are shown in these plots to provide a baseline of the acceptable error for the model runs. Figure 1a shows a CIR-driven event that occurred on 14 October 2002. During the main phase of this event, each of the HEIDI run sets stays between the indices until nearly the storm peak. While run set 2 does well to reproduce the peak values, the other run sets do not reach the large-negative values. Run sets 1, 3, and 4 are off by approximately 20 to 40 nT. The degree of error near the peak then leads to error in the beginning of the recovery phase. Then by the late recovery phase, all of the run sets are again approximately within the range of the indices.

Figure 1b describes the MC-driven storm that occurred on 3 October 2001. For this event, the general trend in simulated *DPS** of each run set is similar. The main difference between the data and model is the magnitude of the storm peak. While run set 2 does well reproducing the storm peak described by the three indices, the other run sets do not reproduce the large-negative values. It should also be noted that all of the run sets end at the start of 6 October. The abrupt end coincides with the end of the simulated 4 day interval.

Table 2. The Average Storm Phase Duration for Each Solar Wind Driver Configuration

	All (h)	CIR (h)	CME (h)	MC (h)	Sheath (h)
Main phase	13.72	16.63	13.3	15.88	9.68
Recovery phase	74.95	65.00	76.42	77.13	74.63

Figure 1c shows a sheath-driven geomagnetic storm that occurred on 11 May 2002. During the beginning of the main phase, run set 4 does well reproducing a smoothed version of the three indices. During the later half of the main phase, run sets 2 and 3 do well simulating the decrease to the peak values, while run sets 1 and 4 are off by approximately 20 nT. Another issue is the timing of the *DPS** storm peaks, which occur earlier than that of the three indices.

4. Statistical Results

Superposed epoch analysis is often used to reveal the typical behavior of a set of events [e.g., *Taylor et al.*, 1998]. This study applies a normalized epoch timeline similar to that of *Katus et al.* [2013] and *Katus and Liemohn* [2013]. The definition of the epoch markers starts with the time of the storm peak *Dst*. The end of the recovery phase is then selected as the maximum *Dst* in the following 96 h. Next the maximum *Dst* in the 24 h prior to the storm peak is found to define the main phase. To allow all of the storms to be included, this study does not require identification of a storm sudden commencement (SSC). Therefore, the beginning of the initial phase is defined as the largest increase in *Dst* in the 8 h before the start of the main phase (whether or not this is actually an SSC). While this method of defining the SSC works well [*Katus and Liemohn*, 2013; *Katus et al.*, 2013] in this case the minimum increase required is zero. Finally, the preceding 6 h are concatenated to the beginning of the initial phase to provide information concerning the preliminary state of the magnetosphere. The epoch markers found using this technique are shown as black vertical lines in the three example storms specified in Figure 1. Note that the epoch markers were found using *Dst* but the corrected form of each of the indices is shown. *Dst* was used to define the markers since the storm list was created using that index. The epoch markers are then used to calculate the average duration of each storm phase. The average duration of each storm phase for each category of solar wind driver is provided in Table 2. The averages for all storms are consistent with the values found in *Pulkkinen et al.* [2007], *Ilie et al.* [2008], and *Katus et al.* [2013]. The timeline is then normalized using linear interpolation to either stretch or compress the duration of each storm phase to the average duration. The second column of Table 3 gives the number of storm included in each category used in this study.

Figure 2 shows the *Dst**, *SYM-H**, and *USGS** data density for all of the geomagnetic storms along the normalized epoch timeline with the peak *Dst* between −100 and −150 nT. In each of the plots in Figure 2 the *y* axis is the magnitude of the observationally based index, and the *x* axis is the normalized timeline. In these plots, the plot range is limited from −175 nT to +50 nT, even though a few data extend beyond these limits. The black vertical lines define the epoch markers used to calculate the normalized timeline. These markers define the beginning or end of each storm phase. The color of the plot presents the density of data points in each bin. The bins are each 15 min across the *x* axis and 5 nT across the *y* axis. The mean and median values along the timeline are also shown in black and white, respectively. In Figure 2, all three geomagnetic indices show similar behavior using *Dst* to define the time markers.

Table 3. The Root-Mean-Square Error to *SYM-H**

	Storms	*DPS** 1	*DPS** 2	*DPS** 3	*DPS** 4	*Dst**	*USGS**
All storms	90	35.4 nT	25.1 nT	31.4 nT	28.4 nT	10.7 nT	8.6 nT
CME driven	79	37.5 nT	26.1 nT	32.8 nT	29.4 nT	10.3 nT	8.8 nT
CIR driven	11	15.6 nT	17.8 nT	18.5 nT	21.4 nT	12.7 nT	7.0 nT
CME driven, $Dst > -150$ nT	49	29.9 nT	18.4 nT	25.3 nT	25.7 nT	8.9 nT	8.6 nT
CME with MC driven	32	31.1 nT	28.5 nT	31.7 nT	29.7 nT	10.9 nT	9.2 nT
CME with sheath driven	19	56.3 nT	29.3 nT	43.1 nT	34.9 nT	9.6 nT	9.7 nT
MC driven, $Dst > -150$ nT	23	24.9 nT	20.2 nT	23.7 nT	25.3 nT	9.0 nT	8.38 nT
Sheath driven, $Dst > -150$ nT	12	43.9 nT	16.4 nT	32.3 nT	30.9 nT	9.2 nT	9.9 nT

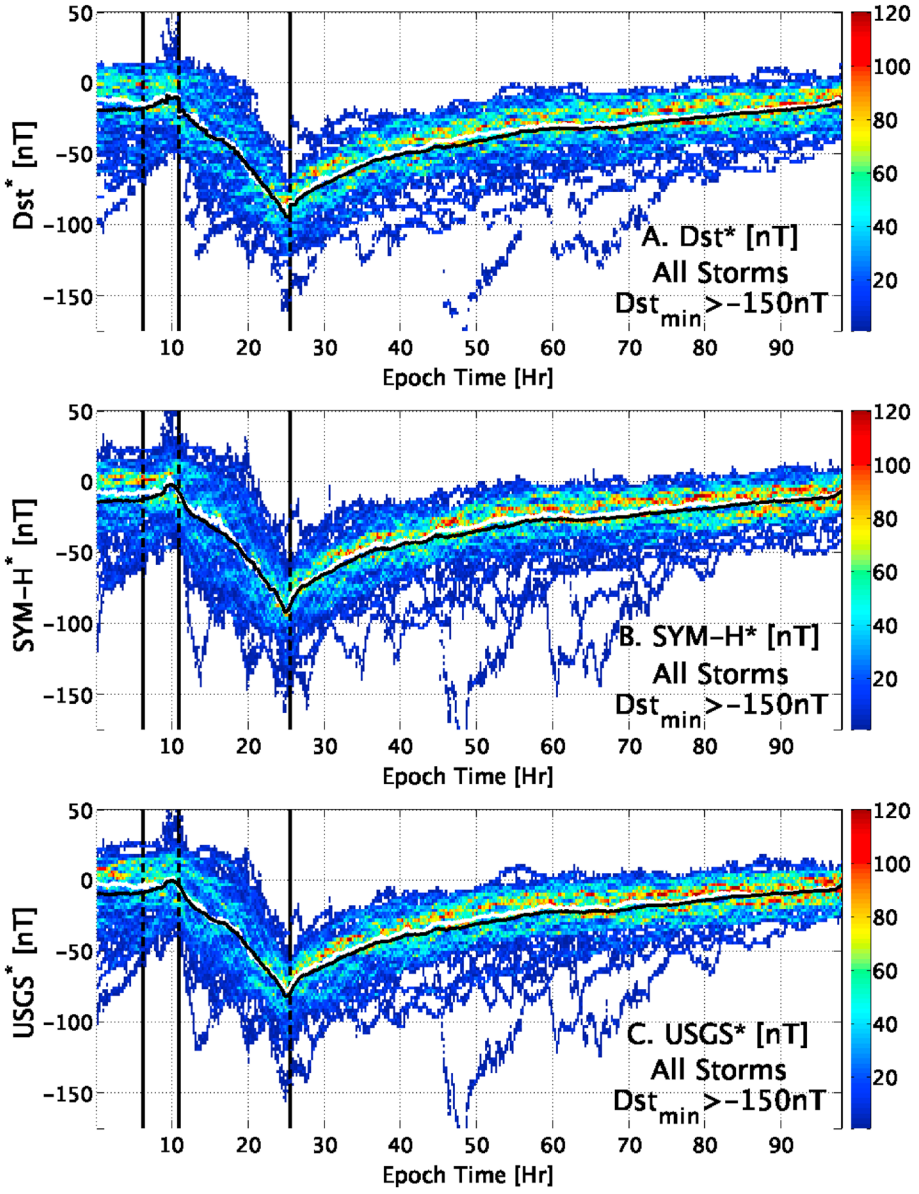

Figure 2. (a) *Dst**, (b) *SYM-H**, and (c) *USGS** for all storms with peak *Dst* between −100 and −150 nT as a function of the normalized superposed epoch timeline. The black vertical lines show the start or end of each phase. The color describes the density of superposed data in 5 nT by 15 min bins. The black and white overlaid provides the mean and median, respectively.

There are a couple of interesting features in Figure 2. First, note the similarity in each of the indices shown in the three plots. The similarity shows good qualitative correlation between the data sets. The similarities and differences of these indices have been addressed in previous studies [e.g., *Wanliss and Showalter*, 2006; *Gannon and Love*, 2011]. *Katus and Liemohn* [2013] analyzed all three indices to provide an uncertainty estimate on the low-latitude perturbation time series. Next note the spread of the data near storm peak. The observed peak *Dst* of most of the storms used in this study are not much less than −100 nT. Finally, note the large variations in the recovery phase. Some of these variations are large enough to be considered additional storm activity. If *Dst* drops below −100 nT, this subsequent event maybe included as another event in the storm list.

The two versions of the outer boundary condition used in the different HEIDI model configurations are shown in Figure 3. These plots remove the spatial resolution from the reanalyzed LANL data by averaging

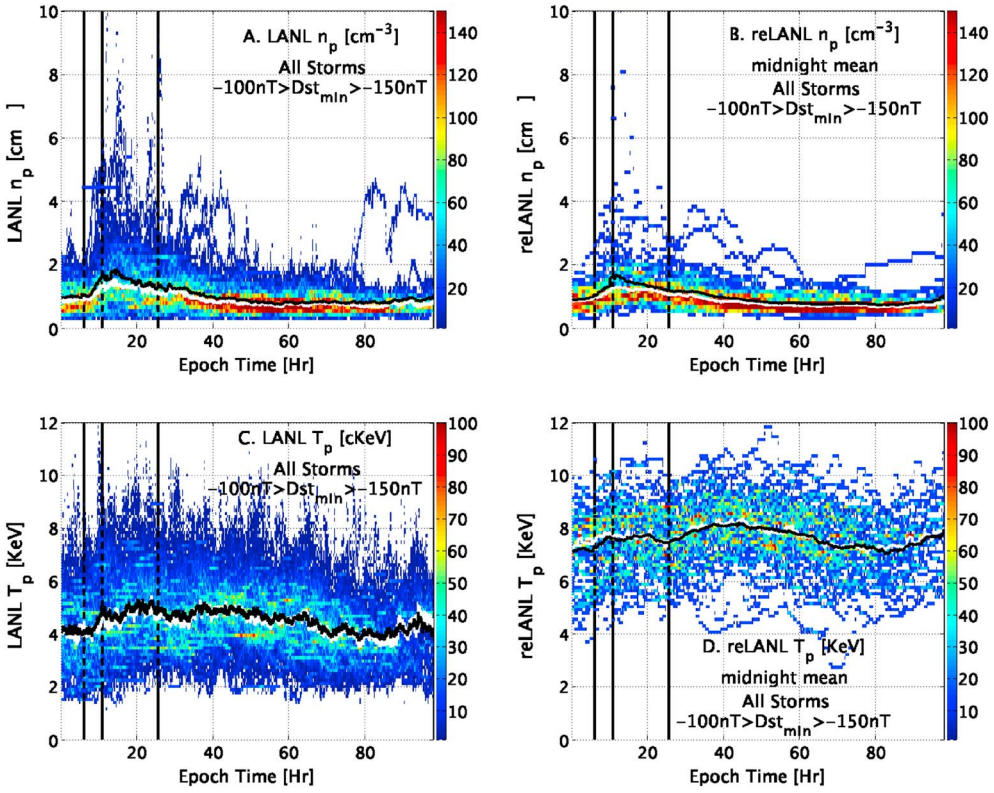

Figure 3. (a) The high time resolution LANL proton density data, (b) the 6 MLT hours around midnight averaged reanalyzed LANL density data, (c) LANL proton temperature, and (d) reanalyzed LANL proton temperature averages for all storms with a peak *Dst* between −100 and −150 nT as a function of the normalized superposed epoch timeline. Figures 3a and 3b show the electron density, and Figures 3c and 3d show the proton density. The black vertical lines show the start or end of each phase. The color describes the density of superposed data in 100 bins along the *y* axis and by 15 min bins along the *x* axis. The black and white overlaid provides the mean and median, respectively.

across the six MLT hours around midnight. Comparison of either density or temperature shows that the LANL data have larger and faster fluctuations than the reanalyzed version. This is consistent with the LANL data having higher time resolution than the reanalyzed version and shows that only the LANL data will be able to describe transient spikes of plasma and energy injections into the inner magnetosphere. Both the mean and the median of the density data follow similar trends. The proton temperatures, on the other hand, do not follow a similar trend or have a similar magnitude for each of the versions of the data. The mean proton temperatures are off by approximately 3 KeV throughout the epoch time of the storm.

Figure 4 illustrates the *SYM-H** data density in the same format as Figure 2, but for the subgroups of ICME- and CIR-driven storms. Figure 4 shows that the magnitude and behavior of the geomagnetic response to CIR- and ICME-driven events are different. The *x* axis is different because the average main phase duration of ICME-driven events (13.3 h) is shorter than that of CIR-driven events (16.63 h), while the average recovery phase duration of ICME-driven events (76.42 h) is longer than for CIR-driven events. All of the superstorms are ICME driven. Furthermore, the color scale is different because only 11 of the intense storms are CIR driven, while 23 are MC driven (with *Dst* between −100 nT and −150 nT) and 12 are SH driven (with *Dst* between −100 nT and −150 nT). The white median line overplotted on the data is difficult to discern, but it follows a similar trend as the other panels of Figure 2 in that it is usually located a few nanotesla higher than the mean during the main phase and early recovery, and is nearly coincident with the mean in the late recovery phase.

The modeled *DPS** data density for the four HEIDI run sets are displayed for CIR-driven events in Figure 5. Each plot follows the normalized timeline as found above from the *Dst* data. Comparison of these simulation results with the *SYM-H** shown in Figure 4a show that the mean peak for CIR-driven storms for

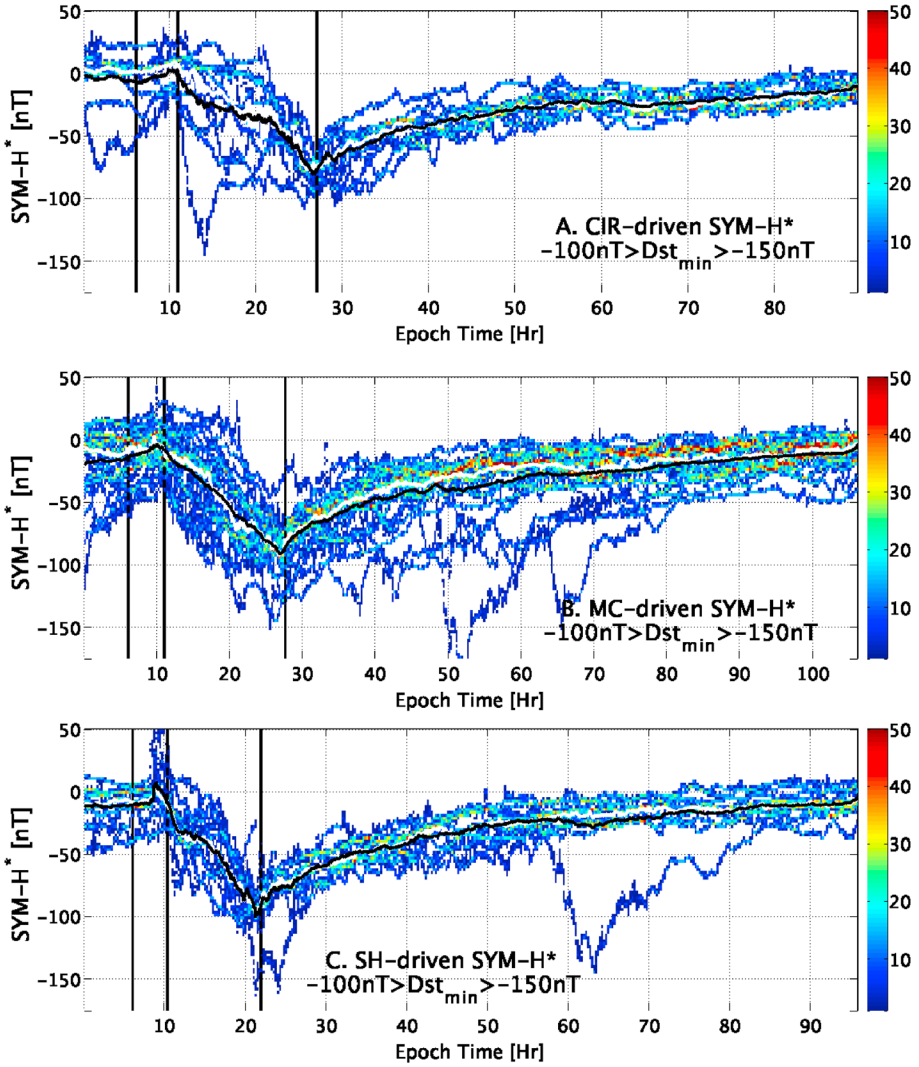

Figure 4. *SYM-H** along the normalized superposed epoch timeline for (a) CIR-driven, (b) MC-driven, and (c) SH-driven storms with peak *Dst* between −100 and −150 nT. The black vertical lines show the start or end of each phase. The color bar describes the density of superposed data in 5 nT by 15 min bins. The black and white overlaid provides the mean and median, respectively.

each of the run sets is less negative than *SYM-H**, with the closest being run set 2 (the self-consistent electric field with the LANL MPA outer boundary). Additionally, the LANL MPA outer boundary condition better replicates the variation in data during the main phase.

Zhang et al. [2007a, 2007b] not only identify the broad category (CME or CIR) but also subdivide the ICME-driven storms according to the segment of the ICME associated with the storm peak. *Liemohn and Jazowski* [2008] used these definitions of the solar wind driver in their analysis of run set 1 results at the peak of the storm. This study progresses further by considering data-model comparisons over the entire storm interval for the two primary categories. Figure 4 shows *SYM-H** where the solar wind structure causing the intense storm peak is either a magnetic cloud (MC) or a sheath (SH). The average duration of the main phase of MC-driven events (15.9 h) is much longer than that for sheath-driven events (9.7 h), while the recovery phase durations are closer in length (77.1 and 74.6 h, respectively). Both types of ICME-driven events show variation in recovery but more so in MC-driven events.

Figure 6 displays the *DPS** data density of the four run sets for the 23 magnetic cloud-driven ICME events with *Dst* between −100 and −150 nT. The figure shows that the mean peak model values are not as negative

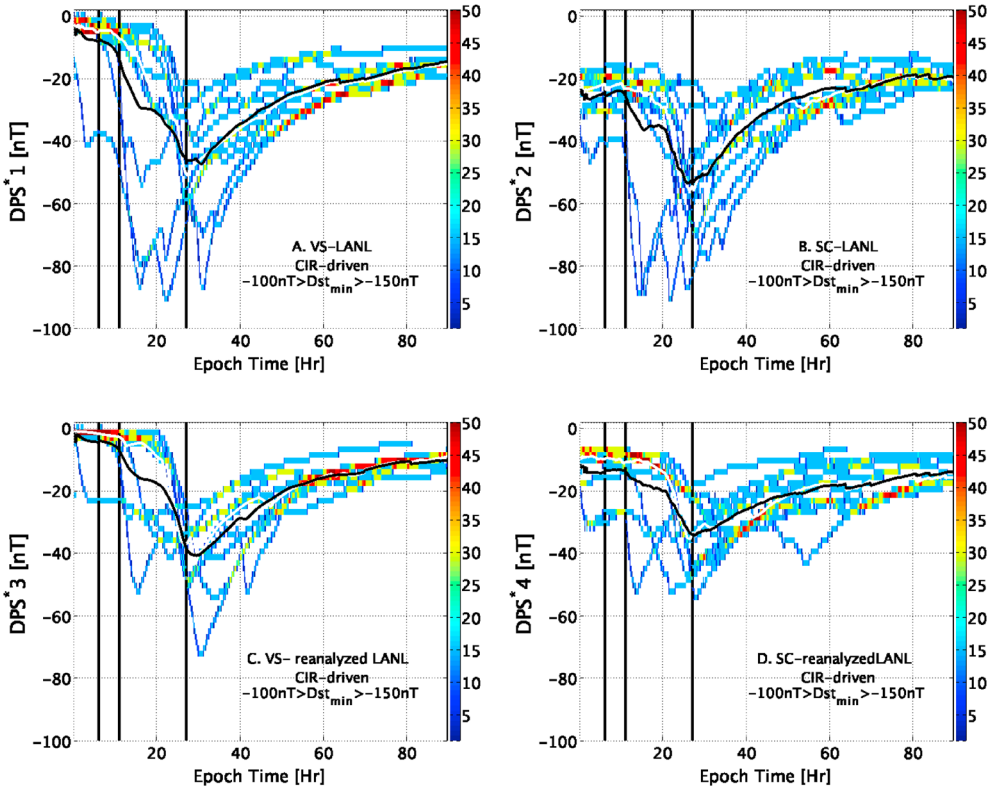

Figure 5. Simulated *DPS** from the four HEIDI run sets for CIR-driven events. The plots have the same setup as Figure 4 but note the *y* axis and color bar scales have changed.

as the observed values. Run set 2 better replicates the larger storms and hence better reproduces the average peak *SYM-H** than the other run sets.

Figure 7 displays the simulated *DPS** data density of the four run sets for the 12 sheath-driven ICME events with peak *Dst* between −100 and −150 nT. Again, the mean peak magnitudes are not as negative as the observed data. As with the MC-driven storms, the run sets using the event-based LANL MPA outer boundary condition better replicate the peak values than the run sets that use the reanalyzed version of the data.

The previous plots describe the observed and simulated geomagnetic disturbances. The plots also highlight when and where the model is doing well for each category of solar wind driver. The remainder of this study preforms a more quantitative examination of the quality of each simulation results for each solar wind driver.

5. Data-Model Comparisons

The root-mean-square error (RMSE) is used to determine the spread of modeled values around the observed values. The RMSE is defined as $\mathrm{RMSE} = \sqrt{\frac{1}{n}\sum_{i=1}^{n}(\hat{y} - y_i)^2}$. Where n is the number of points, y_i is each of the n data points, and $\hat{y}$ is the average of all of the data at this point. In this study the RMSE is used to determine the spread of the simulated *DPS** from each HEIDI run set to the observed *SYM-H**. This analysis is done for the entire storm timeline as well as for each time step along the normalized epoch timeline. The RMSEs between the observed indices provide a baseline observational error when comparing the values between the simulated and observed values. This method allows the quality of the model to be determined throughout each storm phase. That is, we may examine the RMSE at a particular moment in time for a group of storms (n = all of the data at that 10 min time bin) or for the entire storm (n = all data). The RMSE for the entire storm will be referred to as the total RMSE.

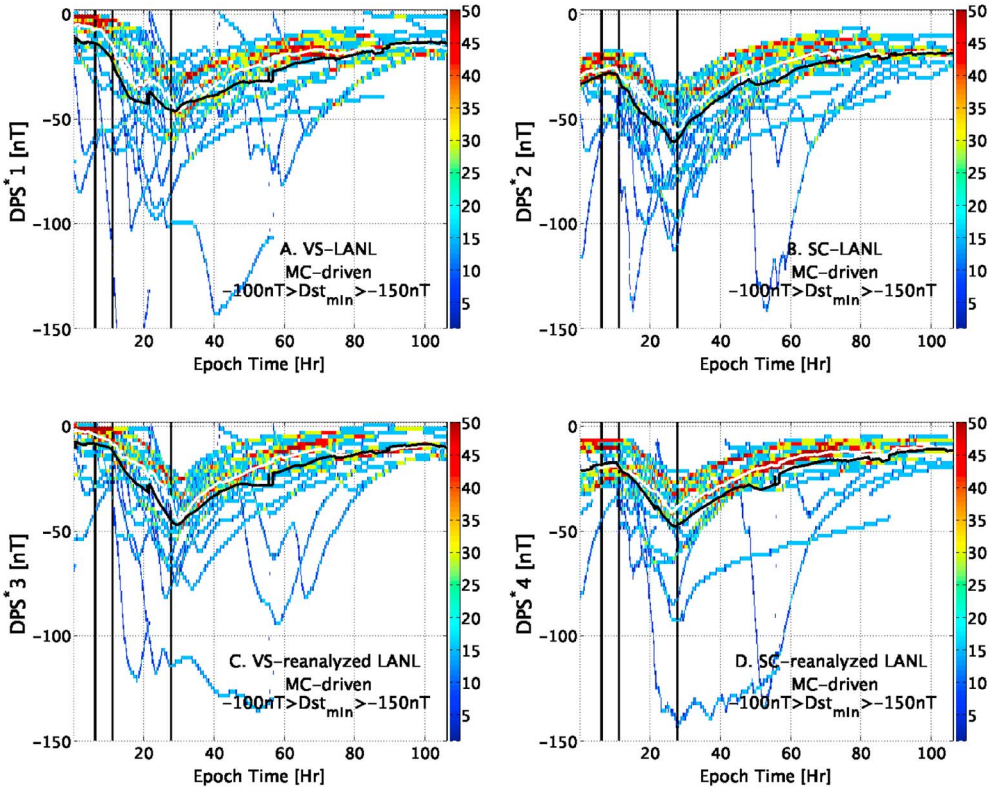

Figure 6. Simulated *DPS** for magnetic cloud-driven ICME events. The figures have the same setup as Figure 5 but note that the scales have changed.

Figure 8 displays the RMSE between *SYM-H** and each of the four model configuration as well as between *SYM-H** and *Dst** and USGS* only for the intense storm events with $Dst_{min} \geq -150$ nT. This range of peak *Dst* values was chosen because all 11 of the CIR-driven storms were within the -100 nT $> Dst_{min} \geq -150$ nT range. The plot on the top compares the CIR-driven events within this range (11 of 11), the middle plot shows the MC-driven events with $Dst_{min} \geq -150$ nT (23 of the 32), and the plot on the bottom presents the sheath-driven events (12 of the 19). In this style of plot, the *y* axis is the RMSE between each data set in nT. The *x* axis is the normalized epoch timeline in hours. The black vertical lines are the epoch markers defining the beginning or end of each storm phase. The different colors define the different data sets being compared.

Examining Figure 8 reveals that, for each of the plots, the RMSE increases approaching the storm peak. Comparing the models confirms that, as in the previous investigation of these storm drivers [e.g., *Liemohn and Katus*, 2012], run set 2 (with the self-consistent electric field and LANL MPA outer boundary condition) has a lower RMSE to *SYM-H* throughout most of the normalized epoch storm timeline. In fact, in the late recovery phase, the RMSE for run set 2 drops below 20 nT for all three driver categories and approaches the data-data error levels of ~10 nT. Additionally, the RMSE is larger throughout most of the storm for sheath-driven events than either CIR-driven or the subgroup of MC-driven disturbances. In particular, the error in the sheath-driven storms is approximately 10 nT larger through the main phase for most of the model configurations to *SYM-H** comparisons than it is for the other solar wind drivers. Furthermore, the RMSE is much larger during the recovery phase for each of the *SYM-H** to model comparison except run set 2. There is also a lot of variation in the RMSE through the recovery phase of the sheath-driven events.

Table 3 lists the total RMSE for each comparison. For now, consider the top row of the table. The RMSE between *SYM-H** with *DPS** 1, 2, 3, and 4 is found to be 35.4, 25.1, 31.4, and 28.4 nT, respectively. The RMSE between *SYM-H** with *Dst** and *USGS** is found to be 10.7 and 8.6, respectively. For all storms, the model run sets that use the self-consistent electric field have a lower RMSE than the Volland-Stern electric field.

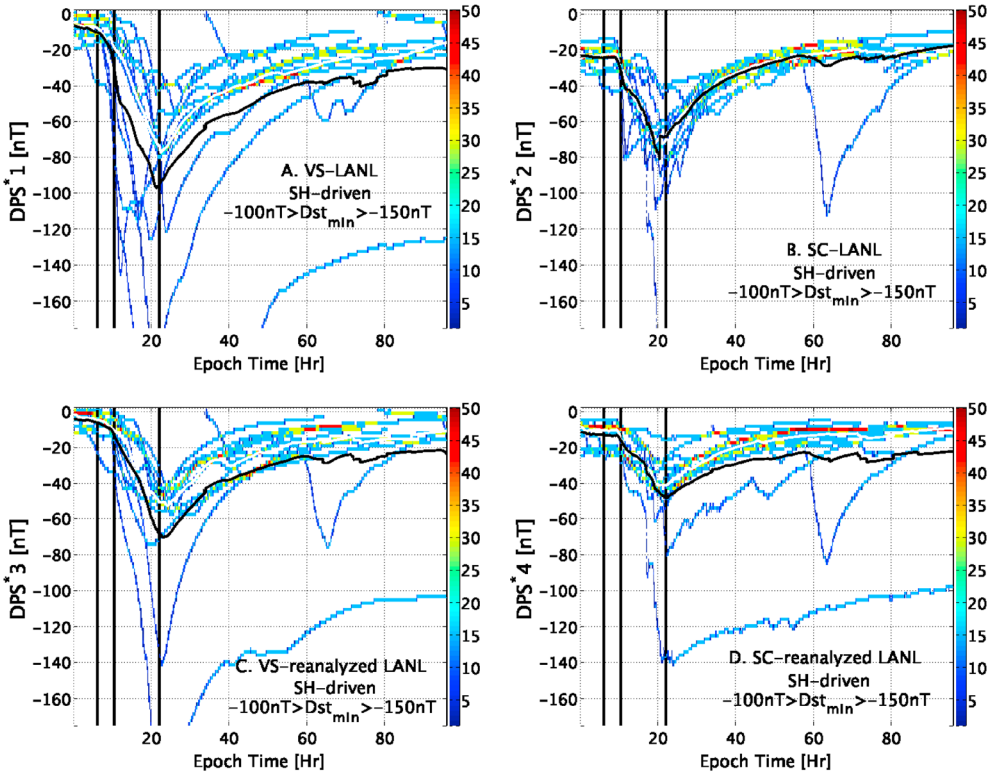

Figure 7. Simulated *DPS** for sheath-driven ICME events. The setup is the same as Figures 4–6 but note that the scales have changed.

Rows 2 and 3 of Table 3 present the total RMSE for each modeled *DPS** to *SYM-H** for each storm driver. For ICME-driven events, the total RMSE for *DPS** 1, 2, 3, and 4 to *SYM-H** is found to be 37.5, 26.1, 32.8, and 29.4 nT, respectively. This is significantly larger than the RMSE values for *SYM-H** to *Dst** (10.3 nT) or *USGS** (8.8 nT). Typically, the RMSE is larger for ICME-driven storms than for all events. The self-consistent electric field has a lower RMSE than the Volland-Stern electric field. The runs using the self-consistent electric field have a lower RMSE when using the LANL MPA data, while the runs using the Volland-Stern electric field have a lower RMSE when using the reanalyzed LANL data.

For CIR-driven events, Table 3 shows that the total RMSE between *SYM-H** and *DPS** 1, 2, 3, and 4 is 15.6, 17.8, 18.5, and 21.4 nT, respectively. These values are not much larger than the RMSE for *SYM-H** to *Dst** (12.7 nT) or *USGS** (7.0 nT). The RMSE for CIR-driven storms is much smaller than the values either for all storms or for ICME-driven events. Unlike the RMSE found for CME-driven events, the RMSE is lower for the Volland-Stern electric field for CIR-driven events. For either electric field, using event-based LANL data for an outer boundary condition results in a lower RMSE than using reanalyzed LANL data.

The total RMSE for each data-to-data and data-to-model comparison is listed in Table 3 for the CIR, MC, and sheath-driven categories subgrouped by requiring that the peak *Dst* must be greater than or equal to −150 nT. The table shows that the RMSE between *SYM-H** and each model configuration, for MC-driven events with $Dst_{min} \geq -150$ nT, is found for run sets 1, 2, 3, and 4 to be 24.9, 20.2, 23.7, and 25.3 nT, respectively. These values are substantially larger than the RMSE for these subsets between *SYM-H** and *Dst** (9.0 nT) and *USGS** (8.38 nT). For the sheath-driven events with $Dst_{min} \geq -150$ nT, the RMSE is found for run sets 1, 2, 3, and 4 to be 43.9, 16.4, 32.3, and 30.9 nT, respectively. Except for run set 2, these values are again much larger than the RMSE for the subsets between *SYM-H** and *Dst** (9.2 nT) and *USGS** (9.9 nT).

Comparing the self-consistent electric field model configurations with each other shows that the event-based LANL MPA outer boundary condition produces a lower RMSE than the reanalyzed version of the data. However, comparing the Volland-Stern electric field run sets shows the opposite result: the reanalyzed LANL

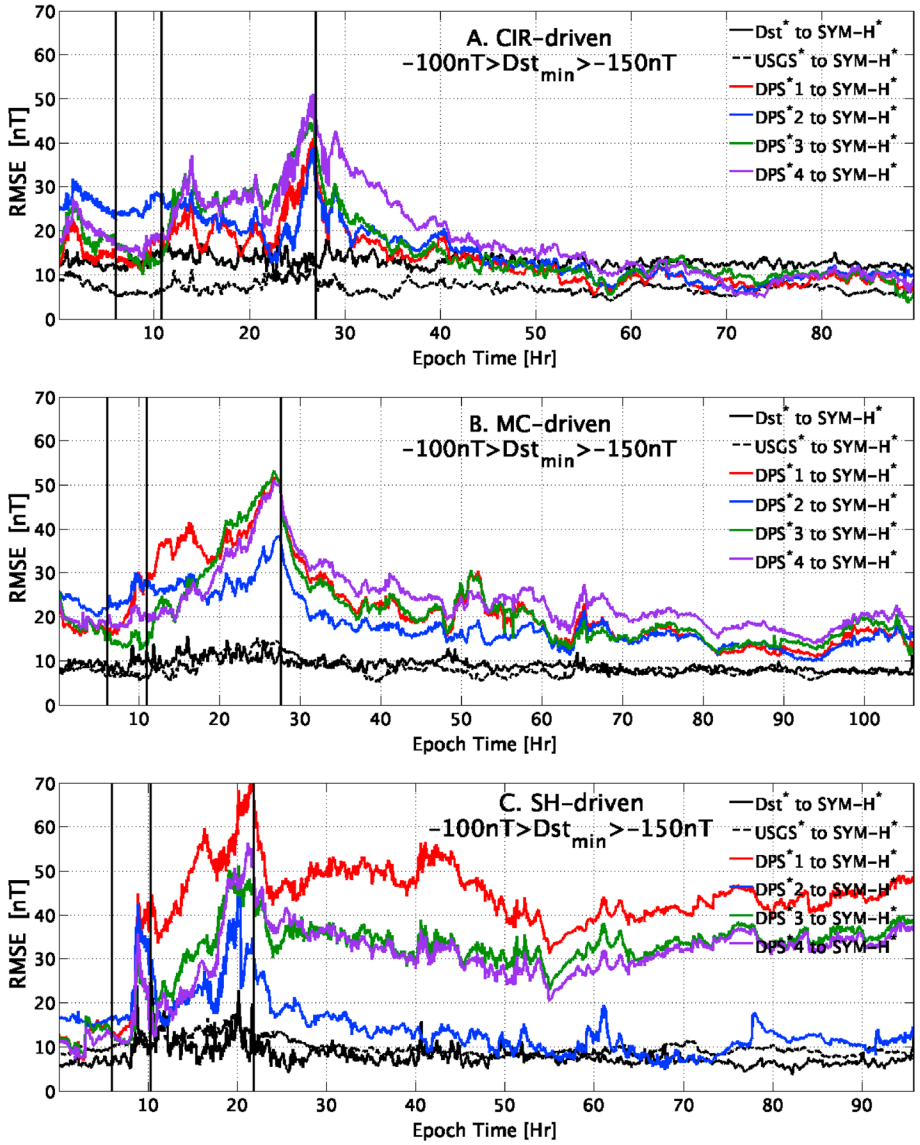

Figure 8. The root-mean-square error (RMSE) as a function of the normalized epoch timeline for (a) CIR-driven, (b) MC-driven, and (c) SH-driven storms with Dst_{min} between −100 and −150 nT.

MPA outer boundary condition produces a lower RMSE. Comparing all of the run sets shows that run set 2, using the self-consistent electric field and the event-based LANL MPA data, consistently has the lowest RMSE.

6. Solar Wind Parameters

To understand the cause of the differences in the solar wind driver, this study examines the dominant solar wind parameters. In particular, the similarity and differences in CIR, MC, and sheath-driven events of the same magnitude are examined. That is, the solar wind parameters for storms with the minimum *Dst* between −100 nT and −150 nT are investigated to remove the dependence of the magnitude of sheath-driven events.

Figure 9 shows the interplanetary magnetic field (IMF) *Bz*, solar wind density, velocity, and temperature for CIR, MC, and sheath-driven events with $-100\ \text{nT} \le Dst_{min} \le -150\ \text{nT}$ along the normalized epoch timeline. In these plots, the timelines are specifically designed for the subgroup of each driver classification and the end of the recovery phase is not shown. The format follows that of the previous plots of this type. The color describes the density of data points. The black vertical lines define the beginning or end of each storm

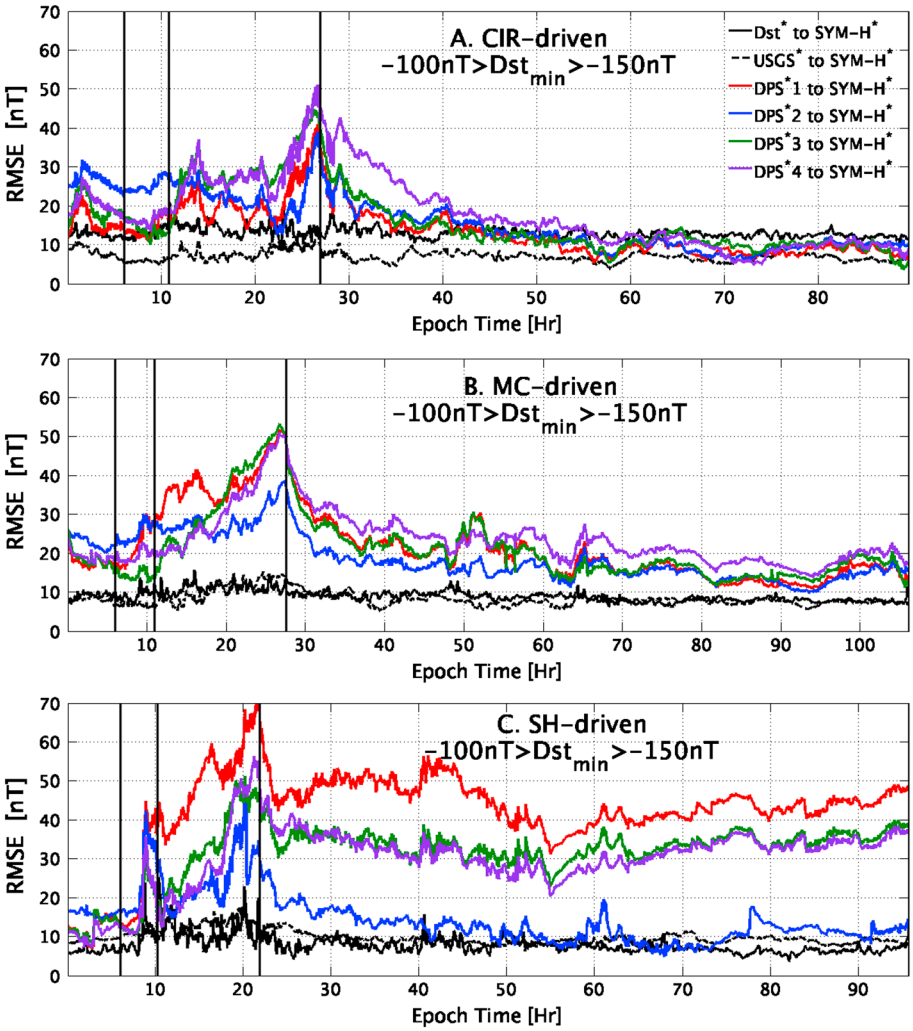

Figure 9. IMF and solar wind parameters for (a) CIR-driven, (b) MC-driven, and (c) SH-driven events. The events are along the normalized epoch timeline but do not show the full recovery phase.

phase. One notable feature of these figures is that the average duration of SH-driven storms is significantly shorter than that of CIR- or MC-driven events.

The IMF *Bz* results are shown in Figures 9a, 9b, and 9c. These plots show that while the IMF *Bz* fluctuates rapidly for all classifications, the average is very close. The magnitude of the fluctuations is larger for the sheath-driven events than for the other categories.

The solar wind density is shown in Figures 9d, 9e, and 9f. These plots show that, prior to the main phase, the density is larger for CIR-driven storms, but sheath-driven storms show a sharp increase at the start of the main phase. The variation in the density then remains larger for sheath-driven events throughout the recovery phase.

The solar wind velocity is shown in Figures 9g, 9h, and 9i. The magnitude of the velocity of sheath-driven events can be 100 s of km/s faster than other categories. This increased velocity can be in the average, which is approximately 100 nT larger. The main difference between the velocity for the two drivers is that, on average, the velocity slowly increases throughout the main phase of CIR-driven events but increases sharply at the beginning of the main phase for MC- and sheath-driven events.

The temperature of the solar wind is shown in Figures 9j, 9k, and 9l. These plots show that the temperature is much larger for CIR- and SH-driven events. This increase in temperature is consistent with a sheath-driven structure that is expected in CIR- and SH-driven storms.

The plots in Figure 9 show us that at 1 AU the solar wind parameters for each category of storm driver can be very different. For sheath-driven events, the IMF *Bz* has larger fluctuations and the solar wind is denser and hotter. The larger southward IMF *Bz* and solar wind velocity are also associated with a larger solar wind electric field (E_y) and cross polar cap potential, which were examined but not shown due to redundancy. The results implicate greater inner magnetospheric convection during the main phase for sheath-driven storms.

7. Discussion

Magnetospheric physics describes the electromagnetism provided by the Earth that protects from solar radiation. In this study we examine the magnetosphere's reaction to several categories of solar structures. While studies have shown that the inner magnetosphere responds differently to CMEs and CIRs during the recovery phase, theory implies that the main phase of sheath-driven CMEs and CIRs should be similar. For both types of events, one would expect to see hot compressed solar wind at 1 AU.

This work inspected the main phase of the three categories of solar wind drivers for the moderately intense ($-150\ \text{nT} \le Dst_{\min} \le -100\ \text{nT}$) that occurred during solar cycle 23. While we were limited to 11 CIR-, 12 sheath-, and 23 magnetic cloud-driven events, the statistical results should describe the typical storm time dynamics of each classification. The storms were simulated using several numerical configurations of the Hot Electron and Ion Drift Integrator (HEIDI). The simulated *DPS**, low-latitude to middle latitude geomagnetic indices, and solar wind parameters are then superpositioned along a normalized storm epoch timeline for various intensity and solar wind driver-based subsets of these events. The density of each type of data was shown to describe the distribution of data along the normalized storm timeline. The root-mean-square error (RMSE) between data sets was given to provide a baseline error along the timeline for each classification of storm driver and intensity. The baseline error was then used to investigate the data-to-model RMSE.

Based on these results, this study agrees with and expands upon the conclusion from *Liemohn and Katus* [2012], which found that for ICME-driven storms the self-consistent electric field better replicates the data than the Volland-Stern electric field. In contrast, for CIR-driven storms the Volland-Stern electric field does better. That is, ICME-driven events are associated with a more internally structured electric field than CIR-driven storms. This study expands upon the previous result by showing that the mean peak of the modeled *DPS** is much less negative than the mean peak of the data. Furthermore, the RMSE is smaller throughout the main and recovery phases of CIR than ICME-driven events. In fact, for CIR-driven events the data-to-model RMSE for each model configuration is close to the data-to-data RMSE throughout the normalized storm timeline. For ICME-driven events, the RMSE is much higher during the recovery phase than it is for CIR-driven storms. In particular, the RMSE is much higher for the Volland-Stern electric field for these ICME-driven events. The results also show that using the event-based LANL data for an outer boundary condition produces more negative peak *DPS** results than using the reanalyzed version of the data. Examination of the outer boundary conditions shows that the LANL data produces better model results. This may be because the reanalyzed data are not adequately describing the proton temperature.

8. Conclusion

This study shows that the inner magnetosphere responds differently to these two different storm drivers. For ICME-driven events, one of the HEIDI run sets is clearly better than the others, while for CIR-driven events, a different run set is the best. This is true not only during the recovery or at the storm peak but throughout the main phase. Run set 2 is the best for the ICME-driven events for nearly all of the epoch timeline (except for a brief interval in the early recovery phase), while this run set is rarely best for the CIR-driven storm set (only during a brief interval in the late main phase).

Magnetic cloud (MC)-driven events make up most of the ICME-driven storms. Thus, it follows that, for this subgroup, the self-consistent electric field has a lower RMSE to *SYM-H** than the Volland-Stern electric field. The self-consistent electric field better replicates the extremely negative values. Particularly, run set 2 is the only model able to reproduce any extremely large negative peak values and is the best at replicating the mean peak. Additionally, the event-based LANL MPA data result in a lower RMSE than the reanalyzed version. The LANL data resulted in much larger main phase decay and more variation in the recovery phase.

Our findings agree with those of *Liemohn et al*. [2006], which show that because ICMEs are the dominant cause of intense storms at Earth, the model configuration of run set 2 is the best overall choice when using HEIDI to simulate the storm time inner magnetosphere. The other run set configurations are adequate for particular epoch times during particular driving conditions, but in general run set 2, with the self-consistent electric field and event-based plasma outer boundary condition, is the most appropriate first choice for model setup.

Our examination of statistical solar wind parameters shows that sheath-driven events are very different from CIR-driven events throughout the entire storm. Additionally, the model results for the sheath (SH)-driven storms follow the results of MC-driven storms rather than CIR-driven storms. However, the RMSE is much larger for SH-driven events than for MC-driven events through the recovery phase. The large error in the recovery phase is clearly due to insufficient ring current loss for the extremely large storms.

This work shows evidence that CIR-driven storms behave differently from other categories throughout the geomagnetic event. Even when only those ICME-driven events for which the sheath was the primary structure responsible for the storm peak for which the storm peak is the same magnitude as the CIR-driven events is considered, the various HEIDI run sets perform differently in the data-model comparisons for CIR-driven events. This result goes against intuition, because theoretically CIRs are essentially sheaths. There are, however, some significant differences in the solar wind properties of an ICME sheath and a CIR, and these differences lead to fundamental changes in the response of the inner magnetosphere.

9. Future Work

While the HEIDI version and configurations used in this study are adequate for this examination of the response of the ring current to different solar wind driving conditions, it may also limit the quality of the results. That is, the dipole magnetic field along with the fixed outer boundary condition at geosynchronous orbit limits the influence of the near tail currents and induced electric fields. Future work should be done to examine the effect of the tail currents and induced electric fields.

Acknowledgments

The authors would like to thank NASA and NSF for funding this research through various grants (specifically, from NASA via grants NNX08AQ15G, NNX09AF45G, NNX10AQ34C, and NNX11AO60G and NSF through grants ATM-0802705, ATM-0903596, and AGS-1102863), including a NASA Graduate Student Research Program fellowship from Marshall Space Flight Center (grant NNX10AL32H). The authors would also like to thank the Kyoto World Data Center (http://wdc.kugi.kyoto-u.ac.jp/index.html) for providing access to the *Dst* and *SYM-H* indices, United States Geological Survey (http://geomag.usgs.gov/data/indices/) for providing access to the USGS 1 min *Dst*, CDAWeb (http://cdaweb.gsfc.nasa.gov/istp_public/) for access to the solar wind data, and Michelle Thomsen for the LANL geosynchronous data which are available upon request from LANL (http://www.mpa.lanl.gov/index.shtml).

Yuming Wang thanks Qiu-Gang Zong and another reviewer for their assistance in evaluating this paper.

References

Bame, S. J., D. J. McComas, M. F. Thomsen, B. L. Barraclough, R. C. Elphic, J. P. Glore, J. T. Gosling, J. C. Chavez, E. P. Evans, and F. J. Wymer (1993), Magnetospheric plasma analyzer for spacecraft with constrained resources, *Rev. Sci. Instrum.*, *64*, 1026, doi:10.1063/1.1144173.

Belian, R. D., G. R. Gisler, T. Cayton, and R. Christensen (1992), High-*Z* energetic particles at geosynchronous orbit during the great solar proton event series of October 1989, *J. Geophys. Res.*, *97*, 16,897–16,906, doi:10.1029/92JA01139.

Borovsky, J. E., and M. H. Denton (2006), Differences between CME-driven storms and CIR-driven storms, *J. Geophys. Res.*, *111*, A07S08, doi:10.1029/2005JA011447.

Burton, R. K., R. L. McPherron, and C. T. Russell (1975), An empirical relationship between interplanetary conditions and *Dst*, *J. Geophys. Res.*, *80*, 4204–4214, doi:10.1029/JA080i031p04204.

Dessler, A. J., and E. N. Parker (1959), Hydromagnetic theory of geomagnetic storms, *J. Geophys. Res.*, *64*, 2239–2252, doi:10.1029/JZ064i012p02239.

Ebihara, Y., and M. Ejiri (1998), Modeling of solar wind control of the ring current buildup: A case study of the magnetic storms in April 1997, *Geophys. Res. Lett.*, *25*, 3751, doi:10.1029/1998GL900006.

Fok, M.-C., T. E. Moore, J. U. Kozyra, G. C. Ho, and D. C. Hamilton (1995), Three-dimensional ring current decay model, *J. Geophys. Res.*, *100*, 9619–9632, doi:10.1029/94JA03029.

Fok, M.-C., R. A. Wolf, R. W. Spiro, and T. E. Moore (2001), Comprehensive computational model of the Earth's ring current, *J. Geophys. Res.*, *106*, 8417–8424, doi:10.1029/2000JA000235.

Gannon, J. L., and J. J. Love (2011), USGS 1-min *Dst* index, *J. Atmos. Sol. Terr. Phys.*, *73*, 323–334.

Ganushkina, N. Y., M. W. Liemohn, and T. I. Pulkkinen (2012), Storm-time ring current: Model-dependent results, *Ann. Geophys.*, *30*, 177–202.

Gonzalez, W. D., J. A. Joselyn, Y. Kamide, H. W. Kroehl, G. Rostoker, B. T. Tsurutani, and V. M. Vasyliunas (1994), What is a geomagnetic storm?, *J. Geophys. Res.*, *99*, 5771–5792, doi:10.1029/93JA02867.

Greenspan, M. E., and D. C. Hamilton (2000), A test of the Dessler-Parker-Sckopke relation during magnetic storms, *J. Geophys. Res.*, *105*, 5419–5430, doi:10.1029/1999JA000284.

Ilie, R., M. W. Liemohn, M. F. Thomsen, J. E. Borovsky, and J. Zhang (2008), Influence of epoch time selection on the results of superposed epoch analysis using ACE and MPA data, *J. Geophys. Res.*, *113*, A00A14, doi:10.1029/2008JA013241.

Ilie, R., R. M. Skoug, H. O. Funsten, M. W. Liemohn, J. J. Bailey, and M. Gruntman (2012), The impact of geocoronal density on ring current development, *J. Atmos. Sol. Terr. Phys.*, *99*, 92–103, doi:10.1016/j.jastp.2012.03.010.

Iyemori, T. (1990), Storm-time magnetospheric currents inferred from mid-latitude geomagnetic field variations, *J. Geomag. Geoelectr.*, *42*, 1249–1265.

Iyemori, T., T. Araki, T. Kamei, and M. Takeda, (1992), Mid-latitude geomagnetic indices ASY and SYM (provisional) No. 1 1989, Data Analysis Center for Geomag. and Space Magnetism, Kyoto Univ., Kyoto, Japan.

Jordanova, V. K. (2006), Modeling the behavior of corotating interaction region driven storms in comparison with coronal mass ejection driven storms, in *Recurrent Magnetic Storms*: *Corotating Solar Wind Streams*, *Geophys*. *Monogr*. *Ser*., vol. 167, edited by B. Tsurutani et al., pp. 77–84, AGU, Washington, D. C.

Jordanova, V. K., L. M. Kistler, J. U. Kozyra, G. V. Khazanov, and A. F. Nagy (1996), Collisional losses of ring current ions, *J. Geophys. Res.*, *101*, 111–126, doi:10.1029/95JA02000.
Jordanova, V. K., L. M. Kistler, C. J. Farrugia, and R. B. Torbert (2001), Effects of inner magnetospheric convection on ring current dynamics: March 10–12, 1998, *J. Geophys. Res.*, *106*, 29,705–29,720, doi:10.1029/2001JA000047.
Jordanova, V. K., H. Matsui, P. A. Puhl-Quinn, M. F. Thomsen, K. Mursula, and L. Holappa (2009), Ring current development during high speed streams, *J. Atmos. Sol. Terr. Phys.*, *71*, 1093–1102, doi:10.1016/j.jastp.2008.09.043.
Jorgensen, A. M., H. E. Spence, W. J. Hughes, and H. J. Singer (2004), A statistical study of the global structure of the ring current, *J. Geophys. Res.*, *109*, A12204, doi:10.1029/2003JA010090.
Kataoka, R., and Y. Miyoshi (2006), Flux enhancement of radiation belt electrons during geomagnetic storms driven by coronal mass ejections and corotating interaction regions, *Space Weather*, *4*, S09004, doi:10.1029/2005SW000211.
Katus, R. M., and M. W. Liemohn (2013), Similarities and differences in low-to middle latitude geomagnetic indices, *J. Geophys. Res. Space Physics*, *118*, 1–8, doi:10.1002/jgra.2013.
Katus, R. M., M. W. Liemohn, D. L. Gallagher, A. Ridley, and S. Zou (2013), Evidence for potential and inductive convection during intense geomagnetic events using normalized superposed epoch analysis, *J. Geophys. Res. Space Physics*, *118*, 181–191, doi:10.1029/2012JA017915.
Klein, L. W., and L. F. Burlaga (1982), Interplanetary magnetic clouds At 1 AU, *J. Geophys. Res.*, *87*(A2), 613–624, doi:10.1029/JA087iA02p00613.
Kozyra, J. U., and M. W. Liemohn (2003), Ring current energy input and decay, *Space Sci. Rev.*, *109*, 105–131.
Lepping, R. P., J. A. Jones, and L. F. Burlaga (1990), Magnetic field structure of interplanetary magnetic clouds at 1 AU, *J. Geophys. Res.*, *95*(A8), 11,957–11,965, doi:10.1029/JA095iA08p11957.
Liemohn, M. W. (2003), Yet another caveat to the Dessler-Parker-Sckopke relation, *J. Geophys. Res.*, *108*(A6), 1251, doi:10.1029/2003JA009839.
Liemohn, M. W., and M. Jazowski (2008), Ring current simulations of the 90 intense storms during solar cycle 23, *J. Geophys. Res.*, *113*, A00A17, doi:10.1029/2008JA013466.
Liemohn, M. W., and R. Katus (2012), Is the storm time response of the inner magnetospheric hot ions universally similar or driver dependent?, *J. Geophys. Res.*, *117*, A00L03, doi:10.1029/2011JA017389.
Liemohn, M. W., and J. U. Kozyra (2003), Lognormal form of the ring current energy content, *J. Atmos. Sol. Terr. Phys.*, *65*, 871–886.
Liemohn, M. W., J. U. Kozyra, V. K. Jordanova, G. V. Khazanov, M. F. Thomsen, and T. E. Cayton (1999), Analysis of early phase ring current recovery mechanisms during geomagnetic storms, *Geophys. Res. Lett.*, *26*, 2845–2848, doi:10.1029/1999GL900611.
Liemohn, M. W., J. U. Kozyra, C. R. Clauer, and A. J. Ridley (2001a), Computational analysis of the near-Earth magnetospheric current system, *J. Geophys. Res.*, *106*, 29,531–29,542, doi:10.1029/2001JA000045.
Liemohn, M. W., J. U. Kozyra, C. R. Clauer, and A. J. Ridley (2001b), Computational analysis of the near-Earth magnetospheric current system during two-phase decay storms, *J. Geophys. Res.*, *106*, 29,531–29,542, doi:10.1029/2001JA000045.
Liemohn, M. W., A. J. Ridley, D. L. Gallagher, D. M. Ober, and J. U. Kozyra (2004), Dependence of plasmaspheric morphology on the electric field description during the recovery phase of the April 17, 2002 magnetic storm, *J. Geophys. Res.*, *109*, A03209, doi:10.1029/2003JA010304.
Liemohn, M. W., A. J. Ridley, J. U. Kozyra, D. L. Gallagher, M. F. Thomsen, M. G. Henderson, M. H. Denton, P. C. Brandt, and J. Goldstein (2006), Analyzing electric field morphology through data-model comparisons of the geospace environment modeling inner magnetosphere/storm assessment challenge events, *J. Geophys. Res.*, *111*, A11S11, doi:10.1029/2006JA011700.
Liemohn, M. W., M. Jazowski, J. U. Kozyra, N. Ganushkina, M. F. Thomsen, and J. E. Borovsky (2010), CIR versus CME drivers of the ring current during intense magnetic storms, *Proc. R. Soc. London, Ser. A*, *466*, 3305–3328, doi:10.1098/rspa.2010.0075.
Love, J. J., and J. L. Gannon (2009), Revised *Dst* and the epicycles of magnetic disturbance: 1958–2007, *Ann. Geophys.*, *27*, 3101–3131, doi:10.5194/angeo-27-3101-2009.
Lynch, B. J., T. H. Zurbuchen, L. A. Fisk, and S. K. Antiochos (2003), Internal structure of magnetic clouds: Plasma and composition, *J. Geophys. Res.*, *108*(A6), 1239, doi:10.1029/2002JA009591.
Miyoshi, Y., and R. Kataoka (2005), Ring current ions and radiation belt electrons during geomagnetic storms driven by coronal mass ejections and corotating interaction regions, *Geophys. Res. Lett.*, *32*, L21105, doi:10.1029/2005GL024590.
Mulligan, T., C. T. Russell, and J. G. Luhmann (1998), Solar cycle evolution of the structure of magnetic clouds in the inner heliosphere, *Geophys. Res. Lett.*, *25*(15), 2959–2962, doi:10.1029/98GL01302.
Ober, D. M., J. L. Horwitz, and D. L. Gallagher (1997), Formation of density troughs embedded in the outer plasmasphere by subauroral ion drift events, *J. Geophys. Res.*, *102*, 14,595–14,602, doi:10.1029/97JA01046.
O'Brien, T. P., and C. L. Lemon (2007), Reanalysis of plasma measurements at geosynchronous orbit, *Space Weather*, *5*, S03007, doi:10.1029/2006SW000279.
O'Brien, T. P., and R. L. McPherron (2000), An empirical phase space analysis of ring current dynamics: Solar wind control of injection and decay, *J. Geophys. Res.*, *105*(A4), 7707–7719.
O'Brien, T. P., and R. L. McPherron (2002), Seasonal and diurnal variation of *Dst* dynamics, *J. Geophys. Res.*, *107*(A11), 1341, doi:10.1029/2002JA009435.
Pulkkinen, T. I., N. Partamies, K. E. J. Huttunen, G. D. Reeves, and H. E. J. Koskinen (2007), Differences in geomagnetic storms driven by magnetic clouds and ICME sheath regions, *Geophys. Res. Lett.*, *34*, L02105, doi:10.1029/2006GL027775.
Rairden, R. L., L. A. Frank, and J. D. Craven (1986), Geocoronal imaging with dynamics explorer, *J. Geophys. Res.*, *91*, 13,613–13,630, doi:10.1029/JA091iA12p13613.
Ridley, A. J., and M. W. Liemohn (2002), A model-derived storm time asymmetric ring current driven electric field description, *J. Geophys. Res.*, *107*(A8), 1151, doi:10.1029/2001JA000051.
Sckopke, N. (1966), A general relation between the energy of trapped particles and the disturbance field near the Earth, *J. Geophys. Res.*, *71*, 3125–3130, doi:10.1029/JZ071i013p03125.
Stern, D. P. (1975), The motion of a proton in the equatorial magnetosphere, *J. Geophys. Res.*, *80*, 595–599, doi:10.1029/JA080i004p00595.
Sugiura, M., and T. Kamei (1991), Equatorial *Dst* index 1957–1986, IAGA Bull. 40, ISGI Publ. Off., Saint-Maur-des-Fossés, France.
Taylor, J. R., M. Lester, and T. K. Yeoman (1998), A superposed epoch analysis of geomagnetic storms, *Ann. Geophys.*, *12*, 612–624, doi:10.1007/s00585-994-0612-4.
Temerin, M., and X. Li (2002), A new model for the prediction of *Dst* on the basis of the solar wind, *J. Geophys. Res.*, *107*(A12), 1472, doi:10.1029/2001JA007532.
Thomsen, M. F. (2004), Why *Kp* is such a good measure of magnetospheric convection, *Space Weather*, *2*, S11004, doi:10.1029/2004SW000089.
Thomsen, M. F., J. E. Borovsky, D. J. McComas, and M. R. Collier (1998), Variability of the ring current source population, *Geophys. Res. Lett.*, *25*, 3481–3484, doi:10.1029/98GL02633.

Tsurutani, B. T., and W. D. Gonzalez (1997), The interplanetary causes of magnetic storms: A review, in *Magnetic Storms, Geophys. Monogr. Ser.*, vol. 98, edited by B. T. Tsurutani et al., pp. 77–89, AGU, Washington, D. C.

Turner, N. E., et al. (2001), Energy content in the storm time ring current, *J. Geophys. Res.*, *106*, 19,149–19,156, doi:10.1029/2000JA003025.

Volland, H. (1973), A semiempirical model of large-scale magnetospheric electric fields, *J. Geophys. Res.*, *78*, 171–180, doi:10.1029/JA078i001p00171.

Wanliss, J. A., and K. M. Showalter (2006), High-resolution global storm index: *Dst* versus *SYM-H*, *J. Geophys. Res.*, *111*, A02202, doi:10.1029/2005JA011034.

Young, D. T., H. Balsiger, and J. Geiss (1982), Correlations of magnetospheric ion composition with geomagnetic and solar activity, *J. Geophys. Res.*, *87*, 9077–9096, doi:10.1029/JA087iA11p09077.

Yue, C., and Q. Zong (2011), Solar wind parameters and geomagnetic indices for four different interplanetary shock/ICME structures, *J. Geophys. Res.*, *116*, A12201, doi:10.1029/2011JA017013.

Zhang, J., et al. (2007a), Solar and interplanetary sources of major geomagnetic storms ($Dst \leq -100$ nT) during 1996–2005, *J. Geophys. Res.*, *112*, A10102, doi:10.1029/2007JA012321.

Zhang, J., et al. (2007b), Correction to "Solar and interplanetary sources of major geomagnetic storms ($Dst \leq -100$ nT) during 1996–2005", *J. Geophys. Res.*, *112*, A12103, doi:10.1029/2007JA012891.

Zhao, H., Q. G. Zong, Y. Wei, and Y. Wang (2011), Influence of solar wind dynamic pressure on geomagnetic *Dst* index during various magnetic storms, *Sci. Chin. Technol. Sci.*, *54*, 1445–1454.